Atmos. Meas. Tech. Discuss., 5, 4969–5008, 2012
www.atmos-meas-tech-discuss.net/5/4969/2012/
doi:10.5194/amtd-5-4969-2012

Atmospheric Measurement Techniques Discussions

A fast method for the retrieval of integrated longwave and shortwave top-of-atmosphere irradiances from MSG/SEVIRI (RRUMS)

M. Vázquez-Navarro[1], **B. Mayer**[1,2], **and H. Mannstein**[1]

[1]Deutsches Zentrum für Luft- und Raumfahrt (DLR), Institut für Physik der Atmosphäre, Oberpfaffenhofen, Germany
[2]Ludwig-Maximilians-Universität (LMU), Meteorologisches Institut, München, Germany

Received: 22 June 2012 – Accepted: 2 July 2012 – Published: 20 July 2012

Correspondence to: M. Vázquez-Navarro (margarita.vazquez@dlr.de)

Published by Copernicus Publications on behalf of the European Geosciences Union.

Abstract

A new *R*apid *R*etrieval of *u*pwelling fluxes from *M*SG/*S*EVIRI (RRUMS) is presented. It has been developed to observe the top-of-atmosphere irradiances of small scale and rapidly changing features that are not sufficiently resolved by specific Earth radiation budget sensors. Our retrieval takes advantage of the spatial and temporal resolution of MSG/SEVIRI and provides outgoing longwave and reflected shortwave radiation only by means of a combination of SEVIRI channels. The longwave retrieval is based on a simple linear combination of brightness temperatures from the SEVIRI infrared channels. Two shortwave retrievals are presented and discussed: the first one based on a multilinear parameterisation and the second one based on a neural network. The neural network method is shown to be slightly more accurate and simpler to apply for the desired purpose. Both LW and SW algorithms have been validated by comparing their results with CERES and GERB irradiance observations. While being less accurate than their dedicated counterparts, the SEVIRI-based methods have two major advantages compared to CERES and GERB: their higher spatial resolution and the better temporal resolution. With our retrievals it is possible to observe the radiative effect of small-scale features such as cumulus clouds, cirrus clouds, or aircraft contrails. The spatial resolution of SEVIRI is 3 km ×3 km in the sub-satellite point, remarkably better than that of CERES (20 km) or GERB (45 km). The temporal resolution is 15 min (5 min in the rapid-scan mode), the same as GERB, but significantly better than that of CERES which, being on board of a polar orbiting satellite, has a temporal resolution as low as 2 overpasses per day.

1 Introduction

Satellite observation of irradiances (fluxes) is essential for assessing the radiation budget of the Earth and its changes over time. Clouds exhibit a strong influence on the radiation budget by increasing the reflected shortwave irradiance by about 50 W m^{-2}

AMTD
5, 4969–5008, 2012

and reducing the outgoing longwave radiation by about 30 $W m^{-2}$, thus reducing the net energy input of the Earth-atmosphere system by about 20 $W m^{-2}$ (Kiehl and Trenberth, 1997). The cloud radiative effect shows high spatial variability, ranging from 0 in cloud-free areas to its largest values over deep convective systems, where up to 80 % of the incoming solar radiation may be reflected by the cloud, and the outgoing longwave radiation may also be considerably reduced. In the study of the radiation budget, the high variability of clouds in space and time presents a big challenge. While averages, such as the ones mentioned above, may be derived from observations with low spatial and temporal resolution, the study of the radiative effect of individual cloud types requires the highest spatial and temporal resolution currently available. In this paper we present a method, RRUMS, to derive the top of atmosphere irradiances based on SEVIRI, an instrument that presents the best combination of spatial and temporal resolution possible nowadays over the MSG-visible part of the Earth.

Earth radiation budget (ERB) measurements have been typically made by polar orbiting satellites, the temporal resolution of which is not sufficient for the study of the aforementioned rapidly changing clouds processes. ERB data from polar orbiting satellites cannot provide proper temporal sampling, since they lack the multiple views necessary each day to resolve processes on short time scales. Diurnal variations in the radiation budget cannot be monitored with such platforms. In contrast, a geostationary platform allows much better temporal sampling. The GERB instrument (Harries et al., 2005), on board the geostationary satellite MSG, provides irradiance measurements with a high temporal resolution of 15 min since 2004, but its low spatial resolution is still insufficient to resolve smaller structures such as cumuli, cirrus, and aircraft contrails.

The work presented in this manuscript is motivated by the attempt to directly quantify the radiative impact of aircraft contrails and contrail cirrus. In a previous work we described an automatic contrail tracking algorithm (Vázquez-Navarro et al., 2010) which allows the tracking of aircraft contrails through a considerable part of their lifetime. The method proposed here allows – but is not limited to – the determination of the radiative effect of these man-made clouds with the final aim to quantify the total forcing by cirrus

AMTD
5, 4969–5008, 2012

clouds generated or influenced by air traffic. For this purpose both an instrument and algorithm are needed that provide irradiance measurements with very high temporal and spatial resolution. MSG/SEVIRI fulfils both resolution requirements. Moreover, the algorithm must be fast enough to process huge amounts of data.

Previously, there have been several attempts to derive broadband radiances from the SEVIRI narrowband channels. This reflects again the scienfitic necessity for the SEVIRI temporal and spatial resolution. In Clerbaux et al. (2008a,b) two narrowband-to-broadband conversions are described (one for SW, and another one for LW). In a step prior to estimating the irradiances, it is necessary to compute broadband unfiltered radiances from the broadband filtered radiances measured by GERB. Different sets of second-order polynomial regressions based on the narrowband SEVIRI channels (thermal channels for LW and visible channels for SW) were used. The unfiltered radiances estimated are later converted to irradiances using CERES Angular Dependency Models (ADMs). EUMETSAT (2010) released a narrowband to broadband conversion for the Outgoing Longwave Radiation, as a result of a feasibility study. The irradiances are obtained via a regression scheme using the IR and WV SEVIRI radiances and the satellite viewing angle. The product is not operationally derived. The underlying radiation model used both in Clerbaux and in the Eumetsat regressions is SBDART.

The algorithms we have developed are straightforward and fast methods to determine reflected solar radiation and outgoing longwave radiation using only MSG/SEVIRI data. The methods are based on a large set of forward simulations of the MSG/SEVIRI channels. The validations presented in this paper have been carried out by comparing the retrievals with the measurements of widely used instruments such as TERRA/CERES (for example, Loeb et al., 2005, 2007). The more recent instrument MSG/GERB (Harries et al., 2005) has also been used for the validation. The methods are shown to provide reasonably accurate results for our purpose. It can of course not compete with the absolute accuracy of a dedicated radiometer like CERES or GERB,

AMTD
5, 4969–5008, 2012

but together with the improvement in the resolution, the retrieval is excellent for the determination of the instantaneous radiative effect of clouds.

2 Methods

In this section we first briefly describe the satellite instruments used in this study: GERB and SEVIRI on Meteosat Second Generation, and CERES on Terra and Aqua. Then, a description of the model data set (basis of the algorithms) follows. Finally, the retrieval algorithms for the outgoing longwave radiation and reflected shortwave radiation are explained.

2.1 Satellites and sensors

2.1.1 MSG

Meteosat Second Generation (MSG) (Schmetz et al., 2002) is the operational geostationary weather satellite of the European meteorological satellite program. The second generation of Meteosat consists of a series of four spin stabilised spacecraft that will operate consecutively. MSG carries two instruments: the Spinning Enhanced Visible and Infra-Red Imager (SEVIRI) and the Geostationary Earth Radiation Budget (GERB).

GERB

The GERB (Harries et al., 2005) instrument measures broadband solar and thermal radiances which are converted to outgoing longwave and reflected solar irradiances taking into account the cloud properties and surface type detected by SEVIRI to choose the correct angular distribution model (ADM) for each scene. In the shortwave range, some of CERES' ADMs are used (see the CERES description below). For longwave irradiance, a method based on thermal SEVIRI channels is used. It provides for the

AMTD
5, 4969–5008, 2012

first time measurements of irradiances every 15 min and its nadir spatial resolution is 44.6 km × 39.3 km.

SEVIRI

The Spinning Enhanced Visible and Infra-Red Imager (SEVIRI) (Schmetz et al., 2002) combines the advantages of high temporal and high spatial resolution. MSG/SEVIRI, which became operational at the end of January 2004, provides data with a temporal resolution of 15 min. The currently operational MSG (Meteosat-9) observes the "full disk" every 15 min while the back-up satellite Meteosat-8 is operated in "rapid-scan mode" since 2008, which gives a temporal resolution of 5 min for the northern third of the visible hemisphere. SEVIRI comprises twelve spectral bands: four solar, seven thermal infrared, and a mixed solar/thermal channel at 3.9 µm (see Table 1). The spectral coverage of the channels is shown in Fig. 1. The spatial resolution is 3 km × 3 km at the sub-satellite point, except for the high-resolution visible (HRVIS) channel which has a resolution of 1 km × 1 km at the sub-satellite point.

2.1.2 TERRA/CERES

The Clouds and the Earth's Radiant Energy System (CERES) is a broadband scanning thermistor bolometer on board of several polar orbiting satellites (Wielicki et al., 1996), most recently on Terra and Aqua. CERES measures broadband solar and thermal radiances which are converted to irradiances using a sophisticated and well-characterized algorithm. The Angular Distribution Model (ADM) necessary for the conversion, uses scene analysis from the MODIS instrument aboard the same satellites (Loeb et al., 2005, 2007). The spatial resolution of CERES is 20 km at nadir. The CERES data are commonly used to study the radiation budget and have undergone a comprehensive validation.

AMTD
5, 4969–5008, 2012

2.2 Forward model data set

To establish the relationship between MSG/SEVIRI channel radiances and broadband solar and thermal irradiances, a huge set of forward calculations of the eleven MSG/SEVIRI channels (excluding the high-resolution visible channel) plus the corresponding reflected solar and outgoing thermal irradiances was done with the radiative transfer package libRadtran (Mayer and Kylling, 2005). The thermal IR data have already been used and described by Krebs et al. (2007) in order to test the performance of a cirrus cloud detection algorithm. Reflectivities for the three solar channels and equivalent brightness temperatures for the seven thermal SEVIRI channels have been simulated for a wide and extensive range of atmospheric and surface conditions. Clerbaux et al. (2003) followed a very similar approach for the thermal IR.

libRadtran offers a flexible interface to setup the atmospheric and surface conditions as well as a choice of different radiative transfer equation solvers. It has been successfully validated in several model intercomparison campaigns and by direct comparison with observations, e.g. (Van Weele et al., 2000; Mayer et al., 1997). For the simulation of radiances or brightness temperatures in this paper, we selected the DISORT 2.0 solver by Stamnes et al. (1988) with 16 streams because it allows accurate simulations of radiances. Molecular absorption was accounted for by the LOWTRAN atmospheric band model (Pierluissi and Peng, 1985) adopted from the SBDART radiative transfer code (Ricchiazzi and Gautier, 1998) which uses a three-term exponential sum fit with a resolution of 20 cm^{-1}. Each SEVIRI channel is simulated with 15 spectral grid points, weighted with the filter function, and integrated over wavelength.

For our data set we used 10 000 different randomly selected combinations of atmospheric conditions as input:

– profiles of pressure, temperature, water vapour, ozone concentration and other trace gases were taken from the TIGR-3 (Thermodynamic Initial Guess Retrieval) data set (Chevallier et al., 1998);

AMTD
5, 4969–5008, 2012

– since we were specifically interested in ice clouds, each case was calculated with and without ice cloud; the ice cloud optical thickness was varied between 0 and 10, the ice particle effective radius between 10 and 45 µm, with a bottom height between 6 and 10 km and a geometrical thickness of 0.5–2 km; the habit was randomly selected from the six habits provided by Key et al. (2002); Yang et al. (2005);

– 50 % of the cases included a water cloud, with optical thickness between 5 and 50, droplet radius 5–15 µm, cloud bottom height 1–2 km, and cloud geometrical thickness 0.5–2 km;

– the surface skin temperature was calculated by adding a random ±10 K to the temperature of the lowest level of the atmospheric profile and the surface emissivity in the thermal IR was assumed to be 1 in all cases. Some uncertainty might be introduced by this simplification, but emissivities are usually close to 1 in the infrared window region; also, the angular dependence is small: e.g. Sobrino and Cuecas (1999) found relative differences of only 3.3 %, 2.0 %, and 0 % between $\theta_v = 0$ and $\theta_v = 55^\circ$ for water, sand, and grass, respectively; for larger viewing zenith angles, the differences increase further;

– for the calculation of the spectral BRDF (bi-directional reflectance distribution function) in the solar range, 50 % of the cases were over ocean and 50 % were over land. Over ocean, the BRDF was described by the well-established parameterization by Cox and Munk (1954) and Nakajima and Tanaka (1983). The wind speed was varied randomly between 1 and 15 $m\,s^{-1}$. For the remaining 50 % over land we used spectral land surface BRDFs for various surfaces where the spectral albedo was taken from randomly sampled MODIS pixels over woodland, grassland, snow, and desert and the angular distribution was described using the analytic formula by Rahman et al. (1993) with the parameters for the corresponding surface types;

AMTD
5, 4969–5008, 2012

– the cosine of the solar zenith angle was varied between 0.2 and 1.0, corresponding of a solar zenith angle between 0 and 78°.

For each atmospheric data set, brightness temperatures were calculated for satellite zenith angles between 0 and 78°, in equidistant steps of 0.02 in the cosine of the satellite zenith angle and 10° in the relative azimuth. A total of 7 790 000 data points were obtained in the solar spectral range (779 viewing angles for 10 000 atmospheric conditions), and 410 000 in the thermal spectral range (41 viewing angles for 10 000 atmospheric conditions – the relative azimuth does not matter in the thermal). This test data set covers a wide range of atmospheric and surface conditions and forms an ideal basis for determining the relationship between satellite observations and TOA solar and thermal irradiances.

2.3 Retrieval algorithms

RRUMS uses 10 SEVIRI channels (excluding the HRVIS and the mixed solar-thermal 3.9 µm channel) in order to determine solar and thermal irradiance at top of atmosphere. In contrast to the above mentioned retrievals by CERES and GERB it does not explicitely use information about the scene provided by additional sensors. However, some information on the scene type is of course inherently delivered by the spectral information of the SEVIRI channels and enters into the retrieval. The rationale for not using a scene classification was that SEVIRI itself includes enough information about the scene which should be implicitely considered by our algorithm. For the thermal irradiance a simple linear combination of the seven thermal-infrared SEVIRI channels proved to be accurate enough (see Sect. 3). We actually did some scene classification by distinguishing between cases with and without ice clouds. For the solar irradiance we tried both a linear combination and a neural network. Both approaches are based on the three shortwave channels (VIS006, VIS008 and IR_016). The neural network turned out to be more convenient than the linear approach since for the latter we would have required, in addition to the cirrus discrimination, a cloud classification to separate

AMTD
5, 4969–5008, 2012

between cases with and without low clouds. The neural network implicitely "knows" about the cloud type from the SEVIRI channels. "Knows" is probably too strong but one could say that the neural network takes best advantage of the available information and applies the optimum ADM.

Below, we describe the outgoing longwave radiation (OLR) retrieval algorithm and both reflected solar radiation (RSR) approaches, followed by a discussion on the most suitable RSR method.

2.3.1 Outgoing longwave radiation, OLR

According to Stefan-Boltzmann's law, the irradiance emitted by a blackbody is proportional to the fourth power of its temperature. For the fit of the thermal irradiance we therefore decided on the following form:

$$F_{\mathrm{LW}} = \sigma \left(a_0(\theta_{\mathrm{v}}) + \sum_{i=5}^{11} a_i(\theta_{\mathrm{v}}) \cdot T_i \right)^4 \quad (1)$$

where the sum is over the seven thermal channels of MSG/SEVIRI (see Table 1) and T_i are the respective brightness temperatures. The reason for using brightness temperatures rather than absolute radiances was that the former are less dependent on the exact shape of each filter function and the fit may therefore be applied to all four SEVIRI instruments of the Meteosat Second Generation series. Alternatively, one could have used the radiance integrated over each filter function, which would be a more direct indicator of the contribution of each channel to the total integrated radiance, but which implies that the filter functions for each respective SEVIRI instrument are known precisely and that specific fit coefficients are determined for each SEVIRI instrument. Finally, one could have used spectral radiances normalized to wavelength interval as an alternative. Our choice of brightness temperatures gave accurate results, see below.

The fit coefficients $a_i(\theta_{\mathrm{v}})$ were determined by minimising the mean square difference between fitted and actual irradiances for the whole forward model data set. The

AMTD
5, 4969–5008, 2012

parameters have been calculated as function of the satellite (or viewing) zenith angle θ_v in equidistant steps of 0.02 in the cosine of the satellite zenith angle. Since we were particularely interested in cirrus clouds, different coefficients were used for cirrus-free and cirrus-covered scenes. MeCiDA (Meteosat Cirrus Detection Algorithm) by Krebs et al. (2007) is used for the discrimination. Figure 2 shows as an example the coefficients for the 10.8 µm (top) and 12.0 µm (bottom) channels, with (left) and without (right) cirrus clouds, as a function of satellite zenith angle. The strong dependence on satellite zenith angle, the positive as well as negative coefficients, and the strong difference between the cases with and without cirrus should be noted. Interestingly, these coefficients are very robust: we found nearly identical sets of coefficients when we randomly selected only one tenth of the forward model data set. Without even trying to interpret the physical meaning of these parameters, one could infer from the positive and negative signs that the linear fit takes advantage of channel differences which are often exploited for cloud remote sensing, see e.g. Krebs et al. (2007).

Figure 3 illustrates the agreement between the "true" OLR and the fit according to (1). While the agreement for cirrus-free cases is generally good (upper plot; RMS difference 1.7 $W m^{-2}$), the deviation is considerably larger for cases with cirrus clouds (lower plot, RMS difference 2.5 $W m^{-2}$). To further investigate this behaviour we separated the data set into 8 ranges of satellite viewing angles $\mu_v = \cos\theta_v$, from 0.2–0.3, 0.3–0.4,..., 0.9–1.0. Figure 4 clearly shows that the agreement is best for viewing angles around 50° ($\mu_v = 0.6, \ldots, 0.7$; RMS difference 1.3 $W m^{-2}$) while the differences increase by more than a factor 3 towards larger viewing angles ($\mu_v = 0.2, \ldots, 0.3$: RMS difference 4.6 $W m^{-2}$). This implies that best results are to be expected for areas such as Central Europe where the viewing angle of Meteosat is between 50° and 60°.

To explain this behaviour, we looked at the variability of the integrated thermal radiance for a given OLR as a function of viewing angle. This basically illustrates the variability of the angular distribution model (see e.g. Loeb et al., 2003) for a given angle. Please note that, in contrast to other procedures to derive OLR from narrow band radiances, we do not distinguish between the narrowband-to-broadband conversion (which

AMTD
5, 4969–5008, 2012

converts from narrowband radiances to integrated thermal radiances) and the angular distribution model which converts from radiance to irradiance. Rather, both steps are combined in Eq. (1). If the variability of the radiances is large for a given OLR, then we expect a large uncertainty in the derived irradiances. Figure 5 shows the ADM, that is, the ratio of radiance L and OLR E multiplied by π:

$$\mathrm{ADM} = \frac{\pi L(\theta_\mathrm{v})}{E} \tag{2}$$

For a perfectly isotropic thermal irradiance we would get a constant value of 1. In contrast, the graph shows a decrease of radiance with increasing viewing angle, θ_v, which is to be expected for an atmosphere where the temperature decreases with height: with increasing viewing angle the slant optical thickness along the line-of-sight increases; this causes a shift of the effective thermal emission towards higher altitudes and thus, lower temperature. More important for our application, however, is the fact that the variability of the radiance for the cases with cirrus clouds is considerably larger than for the cases without: the radiance above a thin cirrus can be seen as a mixture of the radiance emitted by the surface and atmosphere or lower clouds and the radiance emitted by the cirrus cloud: the larger the slant optical thickness, the lower the emitting temperature, for this reason one can expect highly non-isotropic radiance for optically thin clouds. This is finally illustrated with Fig. 6 which shows the ratio of the radiances at $\theta_\mathrm{v} = 0$ ($\mu_\mathrm{v} = 1$) and $\theta_\mathrm{v} = 78^\circ$ ($\mu_\mathrm{v} = 0.2$) as a measure of anisotropy; for perfectly isotropic radiance this number would be 1. In reality we find the largest deviation from 1 for a visible optical thickness of about 1. The largest deviations occur obvisouly for semi-transparent clouds, as expected.

The figure suggests that the irradiance retrieval could be improved by including more information about the atmosphere, in particular cloud type, cloud top-temperature, and cloud optical thickness. Scene type classification provided by independent instruments is used e.g. in the CERES retrieval described by Loeb et al. (2000, 2003): in the longwave, scenes are classified into clear, broken, and overcast. Additionally, for the non-overcast cases, the surface type (ocean, land, desert) is taken into account. In our OLR

AMTD
5, 4969–5008, 2012

retrieval we separate only into scenes with and without cirrus clouds. Separating the low clouds did not bring any improvement; neither did the separation into surface types, since in our forward model all surfaces were considered isotropic emitters of thermal radiation (and the anisotropy is small anyway, as discussed above). According to Fig. 6, the uncertainty could be reduced slightly if fit parameters were calculated as function of the cirrus optical thickness. However, we did not consider that in our analysis because (a) an optical thickness retrieval is computationally very expensive compared to the application of Eq. (1) and the cirrus detection, and (b) the retrieved optical thickness is uncertain anyway for semi-transparent cirrus clouds.

An example of the OLR algorithm applied to SEVIRI in comparison with the current available instruments (CERES and GERB) can be seen in Fig. 7. For the sake of easing comparisons, all satellite scenes depicting examples of the OLR and RSR applications in this paper correspond to the area shown in false colour in Fig. 8. It can be seen that while the irradiance values remain virtually the same, there is a strong improvement in the spatial resolution and also in the coverage, when compared to CERES.

2.3.2 Reflected solar radiation, RSR

To retrieve the outgoing irradiance in the shortwave part of the spectrum, or reflected solar radiation, we followed two approaches: a linear fit similar to the thermal irradiance, and a neural network.

Linear fit

As for the thermal fit in Eq. (1), the reflectivity can be written as a weighted sum over the reflectivities in the three shortwave channels, VIS006, VIS008, and IR_016:

$$F_{\mathrm{SW}} = b_0(\theta_{\mathrm{v}}, \theta_{\mathrm{s}}, \Delta\phi, \mathrm{SUR}) + \sum_{i=1}^{3} b_i(\theta_{\mathrm{v}}, \theta_{\mathrm{s}}, \Delta\phi, \mathrm{SUR}) \cdot R_i \qquad (3)$$

AMTD
5, 4969–5008, 2012

The thermal coefficients a_i were only dependent on the viewing zenith angle θ_v. However, due to the nature of the shortwave radiation and its interaction with matter, the solar fit coefficients b_i had to be determined separately for cirrus and cirrus-free cases, for all 41 viewing angles θ_v, for the 19 relative azimuth angles $\Delta\phi$, and for solar zenith angle θ_s intervals of 0.05 in the cosine of the solar zenith angle. SUR stands for surface type where we distinguish between land and water because the BRDF of land and water surfaces are fundamentally different. As discussed for the thermal irradiance, alternatively one could have used the radiance integrated over each filter function instead of the reflectivity, which would have been a more direct indicator of the contribution of each channel to the total integrated radiance, but that implies that the filter functions for each SEVIRI channel are known precisely and that specific fit coefficients are determined for each particular satellite.

Figure 9 shows the comparison between the "true" solar RSR and the linear fit, for cases without (top) and with (bottom) cirrus clouds. It is immediately obvious that the uncertainty is considerably larger than in the thermal spectral range (Fig. 3). In particular, we found a mean bias of less than $1\,W\,m^{-2}$ but an RMS difference of $25\,W\,m^{-2}$ for both cases with and without cirrus clouds. In order to improve the agreement, more information about the scene needs to be included in the retrieval, which would require a careful scene analysis. Calculating two separate sets of coefficients b_i for cases with and without water clouds, the RMS difference was reduced to $18\,W\,m^{-2}$. However, rather than implementing a separate scene analysis like e.g. Loeb et al. (2003) which would increase the computing time for the retrieval, we decided to try a neural network instead of the linear fit.

Neural network

The motivation for using a neural network is that an extra scene classification might not be required. The scene classification would need to rely on the same data anyway (SEVIRI), and the hope is that the neural network should inherently do the scene classification. In the CERES retrieval by Loeb et al. (2005) the scene classification is based

AMTD
5, 4969–5008, 2012

on higher-resolution MODIS data from the same satellite platform. The GERB retrieval uses SEVIRI data for the cloud classification (Harries et al., 2005).

The neural network was trained with the reflectivities VIS006, VIS008, and IR_016 (same as for the linear fit), the viewing zenith angle θ_v, the solar zenith angle θ_s, the relative azimuth $\Delta\phi$, the land/water information, and of course the reflected shortwave irradiance as output. The artificial neural network was set up with only one hidden layer of 200 nodes, and the sigmoid function was applied to both the weighted sum of input and hidden layer nodes. The input data set is presented to the backward error propagation training several times in random order. The performance of the trained network is shown in Fig. 10. Two plots are presented to facilitate comparison with the linear fit approach (shown in Fig. 9). However, it must be noted that a cirrus cloud classification is not necessary for the neural network retrieval.

In the case with cirrus (lower plot), a systematic deviation is observed for the largest irradiances which are underestimated by the neural network. The largest deviations, however, occur at irradiances of approximately 80 $\mathrm{W\,m^{-2}}$. The peak at small values of the RSR corresponds to reflection from cloud-free ocean: the reflectivity of the ocean increases with increasing solar zenith angle, which nearly compensates the decrease of the incident solar irradiance with the cosine of the solar zenith angle. For that reason, in cloud-free conditions the reflected solar irradiance is nearly independent of solar zenith angle, while for cloudy conditions we get the expected decrease of the reflected irradiance with increasing solar zenith angle. Since the neural network sometimes fails detecting thin clouds over the ocean, the cloudless sky irradiance is wrongly assigned to the cloudy case and vice versa. For all other scenes, the neural network is able to represent the modelled data without a substantial bias. The mean deviation of the neural network results from the input model data is 4.5 $\mathrm{W\,m^{-2}}$ and the RMS difference is 33 $\mathrm{W\,m^{-2}}$.

AMTD
5, 4969–5008, 2012

Comparison between linear fit and neural network

The comparison is here illustrated for an area over Europe, Mediterranean Sea, and Africa, including low and high clouds, water, land, desert and mountains/snow (see RGB-false colour composite in Fig. 8). In Fig. 11, the values from both broadband radiometers (GERB and CERES, top) in the different parts of the scene can be visually compared to the two SEVIRI-based RSR retrievals (neural network and linear fit, bottom).

The different footprints are due to either the satellite/instrument footprint, the boundaries of the calculation method applied, or both. It can be seen that both the neural network and the linear fit denote an improvement in spatial resolution. Both approaches provide comparable results. However, visual comparison with CERES and GERB suggests that the neural network results are slightly better, for instance in the lower part of the scene, the area above the Sahara desert where the linear fit retrieves obviously higher irradiances. The SEVIRI-based methods present a better spatial resolution and similar irradiance results to GERB and CERES, especially the neural network retrieval.

More quantitatively, Fig. 12 directly compares the two SEVIRI-based retrievals with the CERES and GERB observations. The linear fit shows two distinct modes, above and below the (dashed) one-to-one reference line. The neural network shows an overall better agreement with the GERB and CERES irradiance measurements. Since the neural network, in addition to providing a slightly better agreement with GERB and CERES, does not require a scene classification into cases with and without cirrus, we decided to use the neural network approach.

3 Validation of RSR and OLR retrieval algorithms

Since the newly developed fast RRUMS methods are based on radiative transfer simulations only, they need to be validated by comparison with independent observations. In

AMTD
5, 4969–5008, 2012

the following we show a comparison with results derived from the CERES and GERB instruments. We have chosen CERES because it is the reference instrument for radiation budget measurements, and GERB because it is the broadband radiometer on board of MSG, so it shares SEVIRI's viewing geometry.

The use of three instruments with three different spatial resolutions required careful handling and processing of the data to avoid loss of information. SEVIRI-derived RRUMS data have a substantially better resolution than CERES or GERB data. For the comparison with CERES, data were first mapped onto a geostationary projection with the same nadir point as SEVIRI. This step was obviously not necessary for GERB. Second, SEVIRI data were mapped onto the poorer resolution grid by averaging the SEVIRI data over the corresponding CERES or GERB pixels.

The results of the comparison with CERES are summarised in Table 2. For each date and wavelength range, CERES data have been plotted against RRUMS data, and have been fitted to a straight line $y = mx$, with the measured CERES irradiance as x, RRUMS-derived irradiance as y, slope m, and correlation coefficient r. The total agreement would correspond to slope 1 and correlation coefficient 1. The SW analysis was of course only done for daytime. The missing data points in the table correspond to nighttime scenes, where only LW was evaluated since SW is zero anyway. It can be seen that, in general, the agreement between the CERES observations and the SEVIRI-based RRUMS is very good, in particular for OLR.

The discrepancies from the total agreement are more relevant in the SW case. Possible causes were analysed by studying the relative differences between CERES and MSG/SEVIRI irradiances as a function of a number of parameters likely to influence the calculations, such as:

- solar zenith angle, to discard instrument artifacts or the influence of the diurnal variability of clouds,
- satellite (MSG) zenith angle, that could be a source of error in the areas observed under extreme viewing geometry,

AMTD
5, 4969–5008, 2012

– time delay between TERRA and MSG overpasses, that may cause artifacts due to the movement of clouds,

– latitude/longitude, that may cause misplacement of clouds when mapping, and

– cloud cover.

These analyses revealed hardly any dependence on any of the parameters studied. A slightly higher relative difference was found over bright areas such as high optically thick clouds or the desert. This could already be anticipated in Fig. 11, where some areas of the desert and some of the cloud structures showed higher SW irradiances than in the CERES or GERB measurements (some of the areas that appear green in GERB or CERES, appear red in the SEVIRI neural network scene). Figure 13, corresponding to the same area, shows the absolute differences between RRUMS-retrieval and CERES (or GERB). A simple comparison with the false colour composite (Fig. 8) shows that the higher relative differences are found around cloudy areas in both LW and SW retrievals, especially along the cloud boundaries.

The slight dependence of the relative difference on cloud cover between the SEVIRI-based RRUMS method and CERES is also observed in Fig. 14. It is possibly due to a combination of the ADM selection, the cloud inhomogeneity, and three-dimensional radiative transfer effects. Also, misplacements of cloud structures can lead to additional errors. It must be noted that, although slightly larger errors were found around cloudy areas, this does not necessarily mean that the RRUMS irradiance computation over such areas is wrong. Even though the mapping in the comparison between SEVIRI and CERES has been carefully performed, it could lead to a misplacement of cloudy structures, particularly for high clouds and/or large viewing zenith angles. Finally, an additional contribution to the increasing errors in these areas lies in the fact that sensors do not observe the exactly same scene due to small time differences: clouds are rapidly changing.

The validation with GERB (see example in Fig. 13 and further comparisons in Table 3) shows also a very good agreement. Missing SW irradiance data in the table

AMTD
5, 4969–5008, 2012

correspond again to nighttime scenes. The standard deviation (RRUMS – GERB) for OLR averaged over all cases was 8 $W m^{-2}$. The average standard deviation amounted up to 37 $W m^{-2}$ for daytime RSR.

Both validations show that the RRUMS OLR and RSR retrieval algorithms for SEVIRI described here provide accurate results for our purpose. The OLR agreed better than 1 % with CERES on average over all test cases. The SW irradiance was higher than CERES or GERB by 5 to 10 %. The deviation from total agreement has been shown to be independent of solar and satellite zenith angles, and to be only slightly dependent on cloud cover. Therefore, the results are suitable for determining small scale variability and diurnal variations, thanks to the high temporal and spatial resolution of the SEVIRI instrument. A further advantage of RRUMS is the fast processing time of the algorithm. Additionally, RRUMS does not require a full scene classification or ADMs for the irradiance retrievals.

4 Conclusions

The RRUMS algorithms described here retrieve OLR and RSR from MSG/SEVIRI. In the longwave range, it has been shown that the developed linear combination of the thermal infrared channels is a reliable method to calculate the OLR. For the SW range, two different approaches have been tested: a linear parameterisation, resembling the LW method, and a neural network. The neural network method provided slightly better results in comparison to CERES and GERB and requires no additional information like a scene classification or cloud mask, thus increasing computational speed.

The retrievals have been compared to measurements from the CERES and GERB broadband radiometers. The validation of RRUMS with the CERES and GERB irradiance data showed excellent agreement in the OLR and a systematic over-estimation in the SW.

AMTD
5, 4969–5008, 2012

Thus, the shortwave and the longwave MSG/SEVIRI-based irradiance retrieval algorithms presented in this paper can be used as a tool to retrieve irradiances taking advantage of the temporal and spatial resolution of the SEVIRI sensor. The irradiances are computed on the SEVIRI pixel grid. Moreover, the computation is fully automatic and very fast. We want to point out again that the purpose of these algorithms is not related to climate monitoring, where more accurate instruments like CERES are available. Rather, this method is specifically developed for determining the radiative effects of small scale features such as cirrus clouds and aircraft contrails, where the spatial and temporal resolutions of CERES and GERB are insufficient. A further advantage is that the only satellite information RRUMS requires are the SEVIRI data. RRUMS is an excellent counterpart to the radiometrically more accurate CERES instrument, when the focus is on the smaller scales.

Acknowledgements. This research was supported by the EU FP6 QUANTIFY project and by the EU FP7 REACT4C project. The authors would like to thank Ulrich Schumann and Klaus Gierens for their very valuable comments and suggestions.

References

Chevallier, F., Cheruy, F., Scott, N., and Chedin, A.: A neural network approach for a fast and accurate computation of a longwave radiative budget, J. Appl. Meteorol., 37, 1385–1397, 1998. 4975

Clerbaux, N., Dewitte, S., Gonzalez, L., Bertrand, C., Nicula, B., and Ipe, A.: Outgoing longwave flux estimation: improvement of angular modelling using spectral information, Remote Sens. Environ., 85, 389–395, doi:10.1016/S0034-4257(03)00015-4, 2003. 4975

Clerbaux, N., Dewitte, S., Bertrand, C., Caprion, D., De Paepe, B., Gonzalez, L., Ipe, A., and Russell, J.: Unfiltering of the Geostationary Earth Radiation Budget (GERB) data, part II: longwave radiation, J. Atmos. Ocean. Tech., 25, 1106–1117, 2008a. 4972

Clerbaux, N., Dewitte, S., Bertrand, C., Caprion, D., De Paepe, B., Gonzalez, L., Ipe, A., Russell, J., and Brindley, H.: Unfiltering of the Geostationary Earth Radiation Budget (GERB) Data, part I: shortwave radiation, J. Atmos. Ocean. Tech., 25, 1087–1105, 2008b. 4972

AMTD
5, 4969–5008, 2012

Cox, C. and Munk, W.: Statistics of the sea surface derived from sun glitter, J. Mar. Res., 13, 198–227, 1954. 4976

EUMETSAT: Outgoing Longwave Radiation Factsheet, EUM/OPS/DOC/09/5176 Edn., 2010. 4972

Harries, J., Russell, J., Hanafin, J., Brindley, H., Futyan, J., Rufus, J., Kellock, S., Matthews, G., Wrigley, R., Last, A., Mueller, J., Mossavati, R., Ashmall, J., Sawyer, E., Parker, D., Caldwell, M., Allan, P., Smith, A., Bates, M., Coan, B., Stewart, B., Lepine, D., Cornwall, L., Corney, D., Ricketts, M., Drummond, D., Smart, D., Cutler, R., Dewitte, S., Clerbaux, N., Gonzalez, L., Ipe, A., Bertrand, C., Joukoff, A., Crommelynck, D., Nelms, N., Llewellyn-Jones, D., Butcher, G., Smith, G., Szewczyk, Z., Mlynczak, P., Slingo, A., Allan, R. P., Ringer, M. A.: The Geostationary Earth Radiation Budget project, B. Am. Meteorol. Soc., 86, 945–960, 2005. 4971, 4972, 4973, 4983

Key, J., Yang, P., Baum, B., and Nasiri, S.: Parameterization of shortwave ice cloud optical properties for various particle habits, J. Geophys. Res., 107, D13, doi:10.1029/2001JD000742, 2002. 4976

Kiehl, J. and Trenberth, K.: Earth's annual global mean energy budget, B. Am. Meteorol. Soc., 78, 197–208, 1997. 4971

Krebs, W., Mannstein, H., Bugliaro, L., and Mayer, B.: Technical note: A new day- and night-time Meteosat Second Generation Cirrus Detection Algorithm MeCiDA, Atmos. Chem. Phys., 7, 6145–6159, doi:10.5194/acp-7-6145-2007, 2007. 4975, 4979

Loeb, N., Parol, F., Buriez, J.-C., and Vanbauce, C.: Top-of-atmosphere albedo estimation from angular distribution models using scene identification from satellite cloud property retrievals, J. Climate, 13, 1269–1285, 2000. 4980

Loeb, N., Manalo-Smith, N., Kato, S., Miller, W., Gupta, S., Minnis, P., and Wielicki, B.: Angular distribution models for top-of-atmosphere radiative flux estimation from the Clouds and the Earth's Radiant Energy System Instrument on the Tropical Rainfall Measurement Mission satellite: part I: methodology, J. Appl. Meteorol., 42, 240–265, 2003. 4979, 4980, 4982

Loeb, N., Kato, S., Loukachine, K., and Manalo-Smith, N.: Angular Distribution Models for top-of-atmosphere radiative flux estimation from the Clouds and the Earth's Radiant Energy System Instrument on the Terra Satellite, part I: methodology, J. Atmos. Ocean. Tech., 22, 338–351, 2005. 4972, 4974, 4982

Loeb, N., Kato, S., Loukachine, K., Manalo-Smith, N., and Doelling, D.: Angular Distribution Models for top-of-atmosphere radiative flux estimation from the Clouds and the Earth's Ra-

AMTD
5, 4969–5008, 2012

diant Energy System Instrument on the Terra Satellite, part II: validation, J. Atmos. Ocean. Tech., 24, 564–584, 2007. 4972, 4974
Mayer, B. and Kylling, A.: Technical note: The libRadtran software package for radiative transfer calculations – description and examples of use, Atmos. Chem. Phys., 5, 1855–1877, doi:10.5194/acp-5-1855-2005, 2005. 4975
Mayer, B., Seckmeyer, G., and Kylling, A.: Systematic long-term comparison of spectral UV measurements and UVSPEC modeling results, J. Geophys. Res., 102, 8755–8767, 1997. 4975
Nakajima, T. and Tanaka, M.: Effect of wind-generated waves on the transfer of solar radiation in the atmosphere–ocean system, J. Quant. Spectrosc. Ra., 29, 521–537, 1983. 4976
Pierluissi, J. and Peng, G.-S.: New molecular transmission band models for LOWTRAN, Opt. Eng., 24, 541–547, 1985. 4975
Rahman, H., Verstraete, M., and Pinty, B.: Coupled surface–atmosphere reflectance (CSAR) model. 2. Semiempirical surface model usable with NOAA advanced very high resolution radiometer data, J. Geophys. Res., 98, 20791–20801, 1993. 4976
Ricchiazzi, P. and Gautier, C.: Investigation of the effect of surface heterogeneity and topography on the radiation environment of Palmer Station, Antarctica, with a hybrid 3-D radiative transfer model, J. Geophys. Res., 103, 6161–6178, 1998. 4975
Schmetz, J., Pili, P., Tjemkes, S., Just, D., Kerkmann, J., Rota, S., and Ratier, A.: An introduction to Meteosat Second Generation (MSG), B. Am. Meteorol. Soc., 83, 977–992, 2002. 4973, 4974
Sobrino, J. and Cuecas, J.: Angular variation of thermal infrared emissivity for some natural surfaces from experimental measurements, Appl. Opt., 38, 3931–3936, 1999. 4976
Stamnes, K., Tsay, S., Wiscombe, W., and Jayaweera, K.: A numerically stable algorithm for discrete-ordinate-method radiative transfer in multiple scattering and emitting layered media, Appl. Opt., 27, 2502–2509, 1988. 4975
Van Weele, M., Martin, T., Blumthaler, M., Brogniez, C., den Outer, P., Engelsen, O., Lenoble, J., Pfister, G., Ruggaber, A., Walravens, B., Weihs, P., Dieter, H., Gardiner, B., Gillotay, D., Kylling, A., Mayer, B., Seckmeyer, G., and Wauben, W.: From model intercomparisons towards benchmark UV spectra for six real atmospheric cases, J. Geophys. Res., 105, 4915–4925, 2000. 4975
Vázquez-Navarro, M., Mannstein, H., and Mayer, B.: An automatic contrail tracking algorithm, Atmos. Meas. Tech., 3, 1089–1101, doi:10.5194/amt-3-1089-2010, 2010. 4971

AMTD
5, 4969–5008, 2012

Wielicki, B., Barkstrom, B., Harrison, E., Lee III, R., Smith, G., and Cooper, J.: Clouds and the Earth's Radiant Energy System (CERES): an Earth observing system experiment, B. Am. Meteorol. Soc., 77, 853–868, 1996. 4974

Yang, P., Wei, H., Huang, H.-L., Baum, B., Hu, Y., Kattawar, G., Mishchenko, M., and Fu, Q.: Scattering and absorption property database for nonspherical ice particles in the near- through far-infrared spectral region, Appl. Opt., 44, 5512–5523, 2005. 4976

AMTD

5, 4969–5008, 2012

Table 1. MSG/SEVIRI spectral channels. VIS = visible, IR = infrared, WV = water vapor.

#	Channel	Nominal (μm)	Wavelength range (μm)
1	VIS006	0.64	0.56–0.71
2	VIS008	0.81	0.74–0.88
3	IR_016	1.64	1.50–1.78
4	IR_039	3.92	3.48–4.36
5	WV_062	6.25	5.35–7.15
6	WV_073	7.35	6.85–7.85
7	IR_087	8.70	8.30–9.10
8	IR_097	9.66	9.38–9.94
9	IR_108	10.80	9.80–11.80
10	IR_120	12.00	11.00–13.00
11	IR_134	13.40	12.40–14.40
12	HRVIS		0.50–0.90

AMTD
5, 4969–5008, 2012

Table 2. Comparison between SEVIRI-based RRUMS retrieval and CERES measurements.

Date 2004	Overpass time (UTC) SEVIRI	CERES	OLR (LW) r	Slope	RSR (SW) r	Slope
2 February	02:15	02:07–02:23	0.95	1.02	–	–
24 March	08:00	08:00–08:13	0.97	0.99	0.96	1.07
8 April	07:30	07:14–07:29	0.96	0.99	0.96	1.08
14 June	11:15	11:00–11:19	0.97	1.00	0.97	1.13
8 July	12:00	12:00–12:08	0.99	1.02	0.98	1.10
13 August	14:45	14:39–14:59	0.70	1.02	0.62	1.11
2 September	12:45	12:38–12:57	0.98	1.02	0.98	1.06
15 October	18:45	18:35–18:59	0.94	1.00	–	–
10 November	21:00	20:50–20:59	0.92	0.99	–	–
22 December	23:30	23:14–23:29	0.90	1.01	–	–

AMTD
5, 4969–5008, 2012

Table 3. Comparison between SEVIRI-based RRUMS retrieval and GERB measurements.

Overpass time (UTC)		OLR (LW)		RSR (SW)	
SEVIRI	GERB	*r*	Slope	*r*	Slope
18 May 2006 08:30	08:35	0.98	1.01	–	–
18 May 2006 11:30	11:27	0.98	1.00	0.97	1.03
20 May 2006 03:00	03:00	0.97	1.01	–	–
22 May 2006 00:15	00:14	0.96	1.01	–	–
25 May 2006 15:00	15:01	0.97	1.01	0.96	1.01
29 May 2006 14:15	14:17	0.97	1.01	0.96	1.03
1 June 2006 06:30	06:25	0.98	1.01	–	–
1 June 2006 12:45	12:41	0.97	1.00	0.95	1.04
1 June 2006 22:00	21:58	0.97	1.01	–	–
3 June 2006 10:00	09:54	0.97	1.00	0.96	1.05
10 June 2006 22:00	22:02	0.97	1.01	–	–
12 June 2006 07:30	07:24	0.98	1.01	0.95	1.04

AMTD
5, 4969–5008, 2012

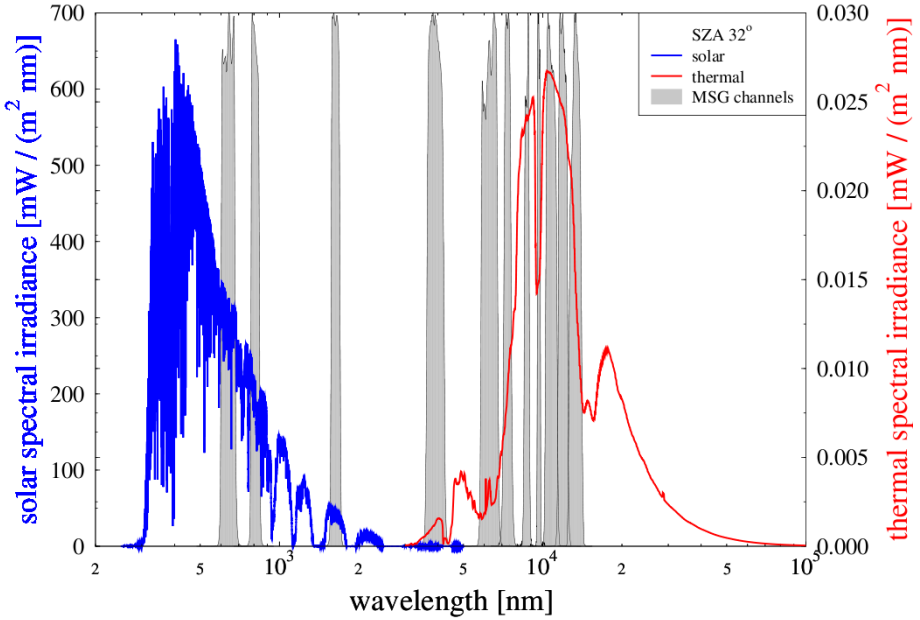

Fig. 1. MSG/SEVIRI spectral channels and an example spectrum of reflected solar and outgoing longwave irradiance.

AMTD
5, 4969–5008, 2012

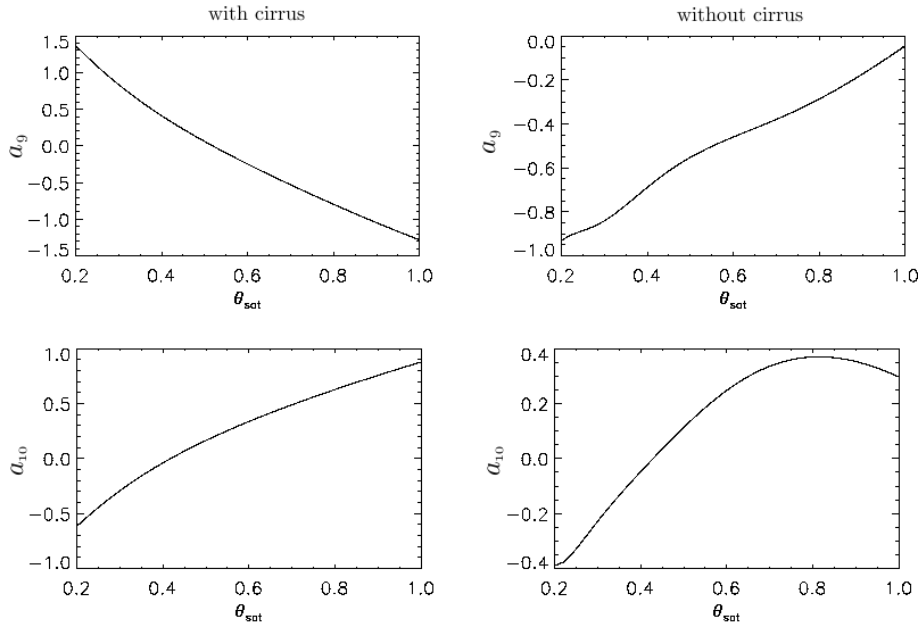

Fig. 2. Fit coefficients corresponding to T_9 (10.8 µm) and T_{10} (12.0 µm) in Eq. (1) vs. satellite viewing angle in the cirrus-free and in the cirrus-covered case. The order of magnitude of the coefficients corresponding to the remaining IR-thermal channels is similar to the ones presented here.

AMTD
5, 4969–5008, 2012

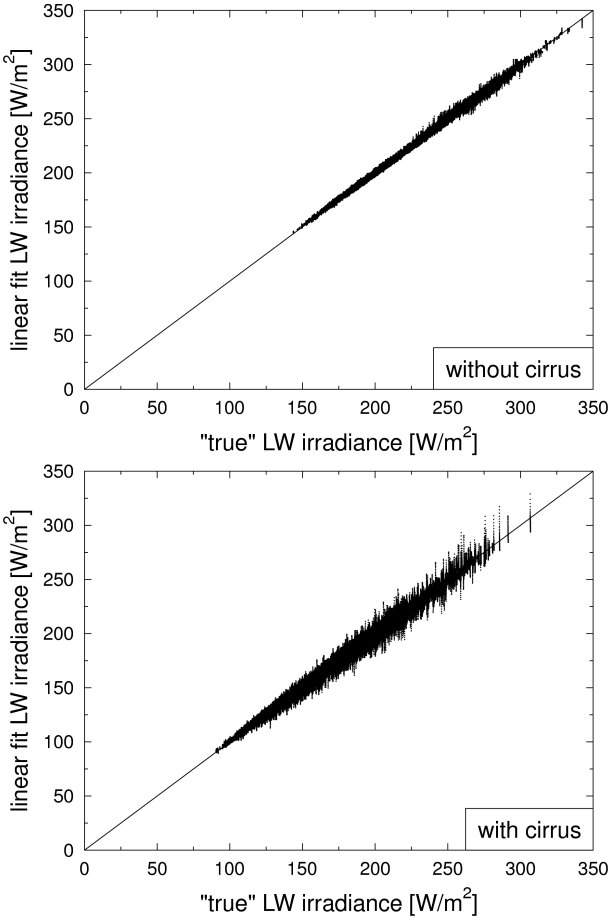

Fig. 3. Comparison between "true OLR" and the linear fit for cirrus-free cases (top) and cases with cirrus clouds (bottom).

AMTD
5, 4969–5008, 2012

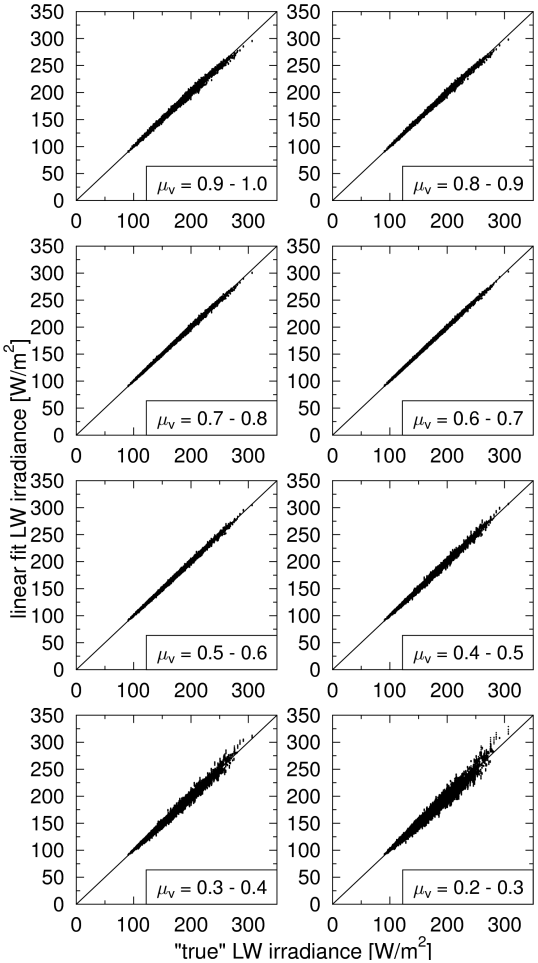

Fig. 4. Same as Fig. 3, but for cases with cirrus clouds and split into several viewing angle ranges.

AMTD
5, 4969–5008, 2012

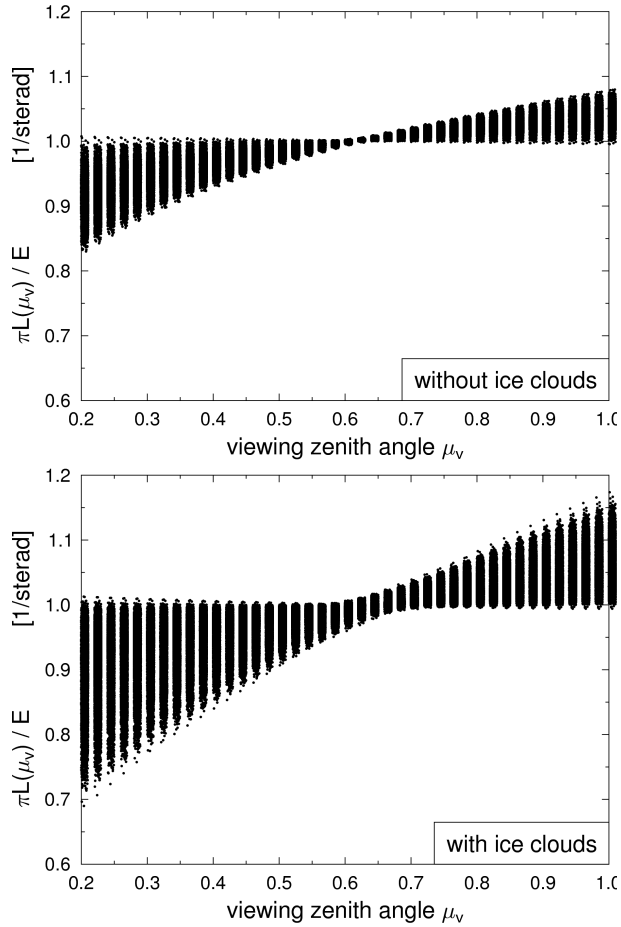

Fig. 5. The ADM (see Eq. 2) as a function of the cosine of the viewing zenith angle $\mu_v = \cos\theta_v$ for cases without (top) and with (bottom) cirrus.

AMTD
5, 4969–5008, 2012

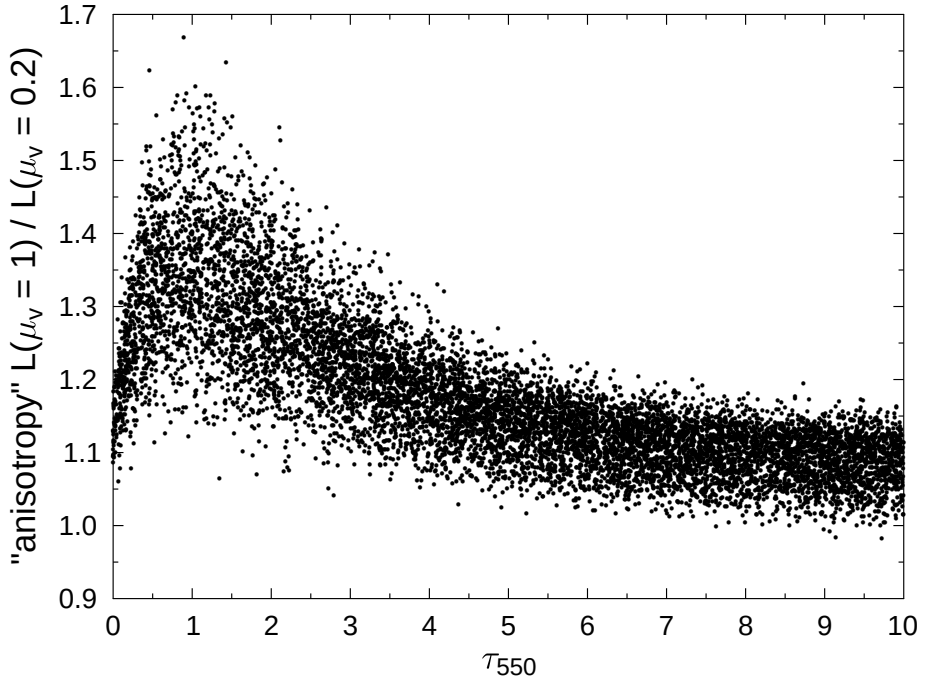

Fig. 6. The "anisotropy", defined as the ratio of nadir radiance and radiance at 78° viewing angle, as function of the visible optical thickness.

AMTD
5, 4969–5008, 2012

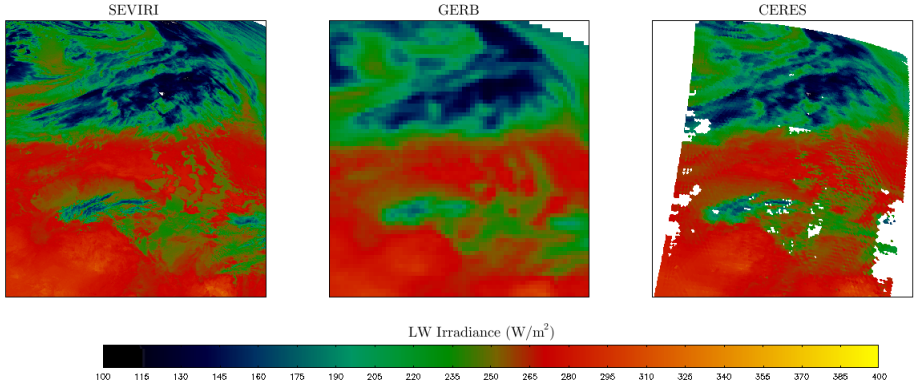

Fig. 7. Comparison between the OLR method based on SEVIRI and the two current irradiance measurement instruments (CERES and GERB). The white areas in GERB and CERES are missing data due to the instrument characteristics. Same scene as Fig. 8.

AMTD
5, 4969–5008, 2012

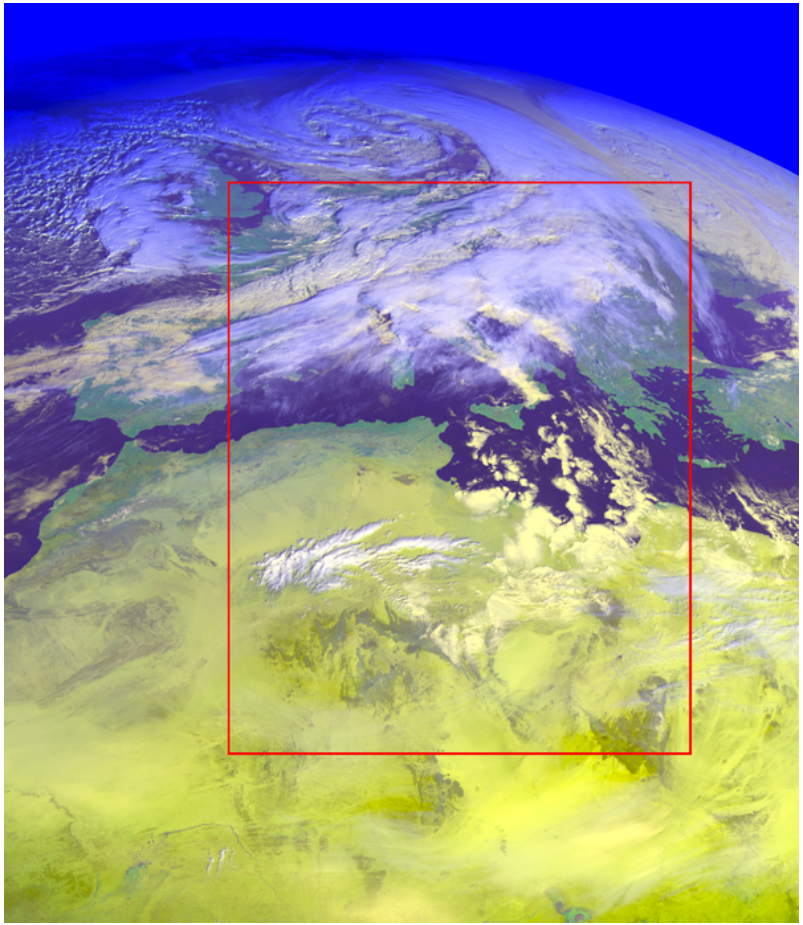

Fig. 8. RGB false colour composite of the area (in red) from SEVIRI corresponding to the comparisons in Figs. 7, 11, 12 and 13. Date and time: 1 January 2007, 10:00 UTC.

AMTD
5, 4969–5008, 2012

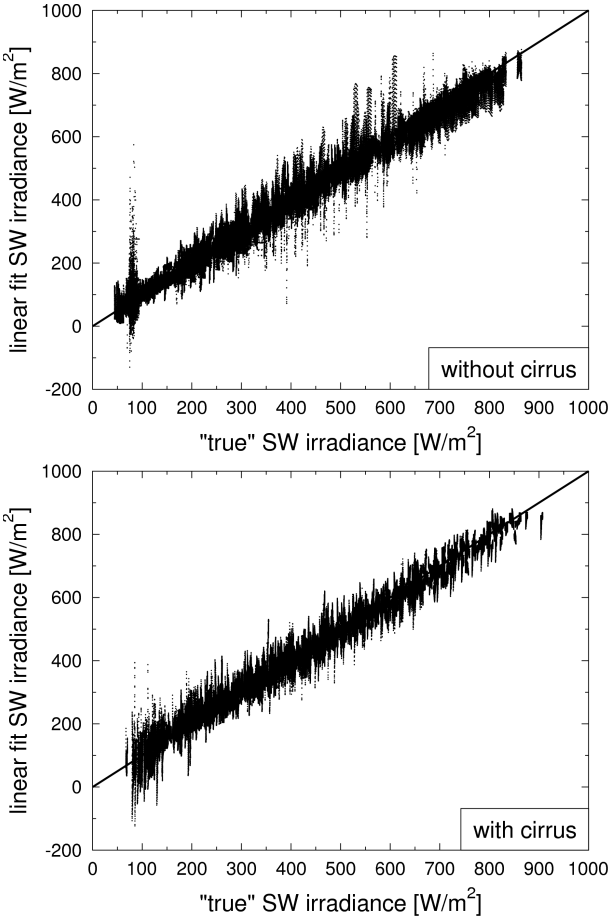

Fig. 9. Comparison between "true" SW irradiance and the linear fit for cirrus-free cases (top) and cases with cirrus clouds (bottom).

AMTD
5, 4969–5008, 2012

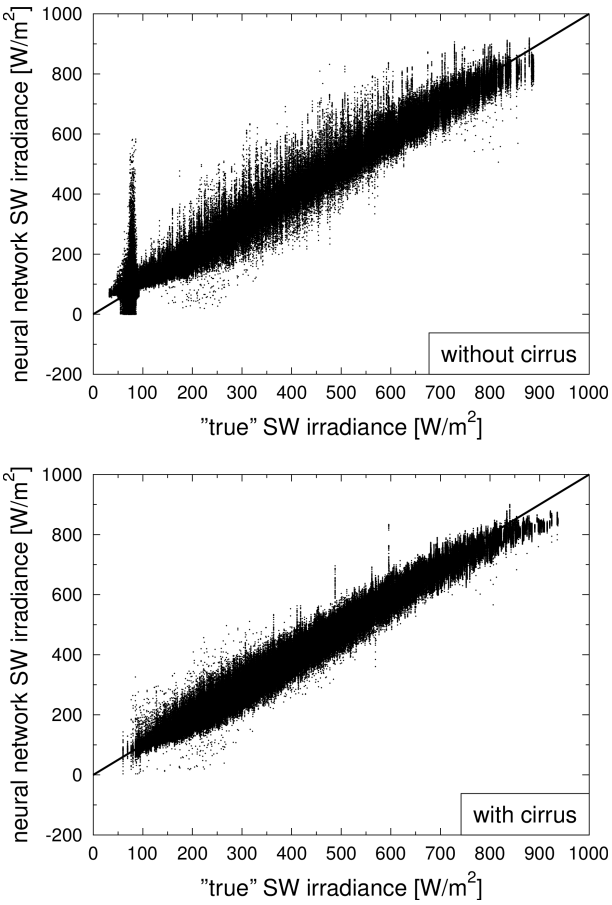

Fig. 10. Comparison between "true" SW irradiance and the neural network retrieval for cirrus-free cases (top) and cases with cirrus clouds (bottom).

AMTD
5, 4969–5008, 2012

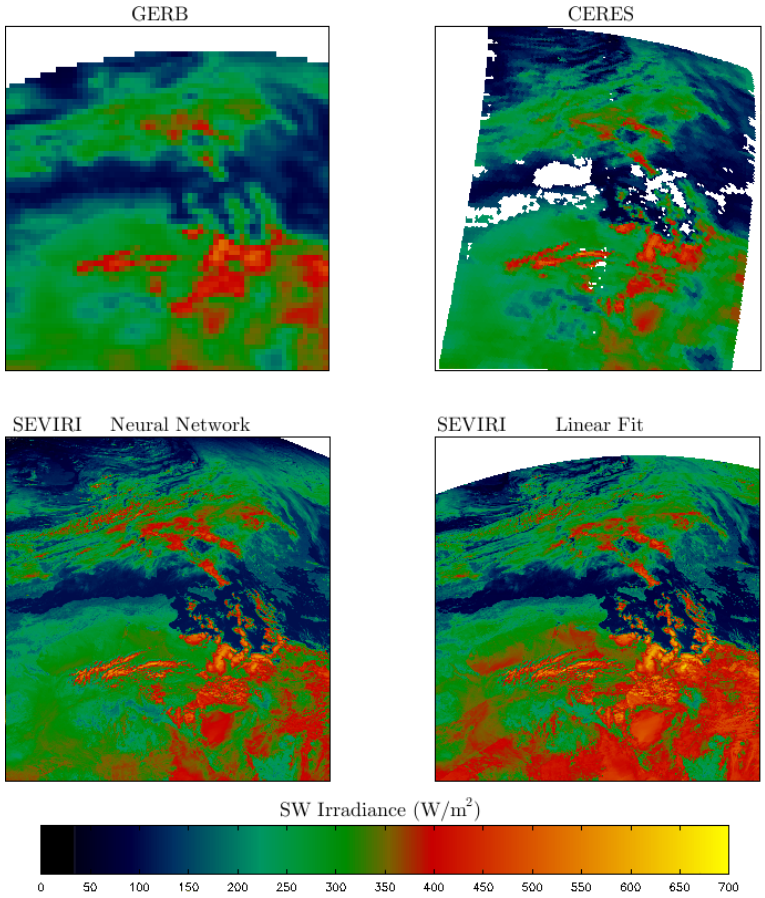

Fig. 11. Comparison between the SW measured irradiances (GERB and CERES) and the two retrieval methods (neural network and linear fit). The corresponding RGB false colour composite can be seen in Fig. 8. The white areas in all plots are due either to the instrument characteristics or to the method constraints.

AMTD
5, 4969–5008, 2012

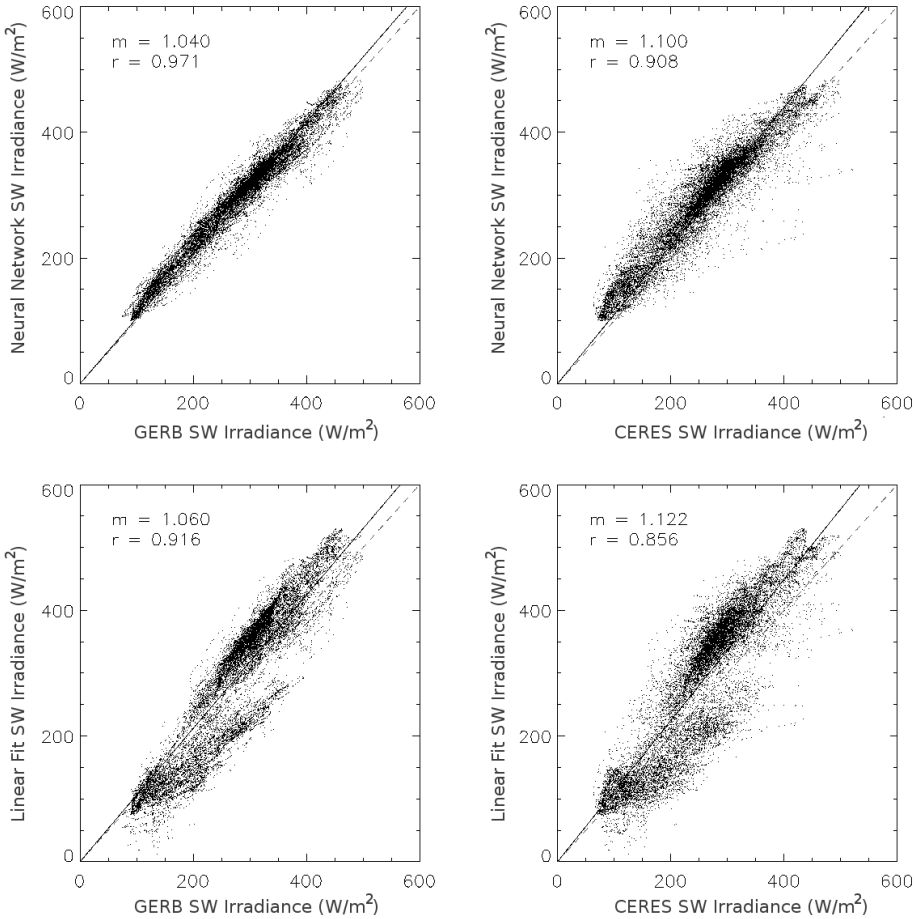

Fig. 12. Comparison between GERB and CERES observations of the RSR and the two retrieval methods (neural network and linear fit) shown in Fig. 11. The solid line corresponds to the linear fit $y = mx$ and the dashed line shows the 1 : 1 ideal behaviour, for reference.

AMTD
5, 4969–5008, 2012

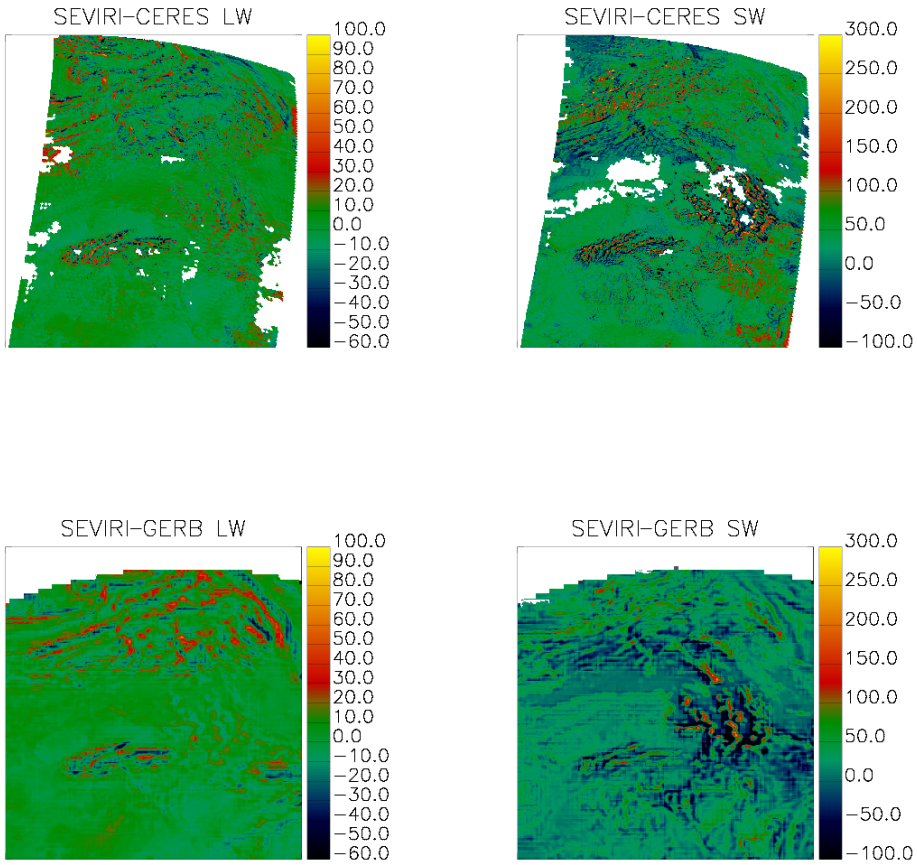

Fig. 13. Absolute differences in $W m^{-2}$ between the SEVIRI-based RRUMS methods and the CERES (top) and GERB (bottom) measurements in both LW (left) and SW (right). The higher differences are found around cloudy areas.

AMTD
5, 4969–5008, 2012

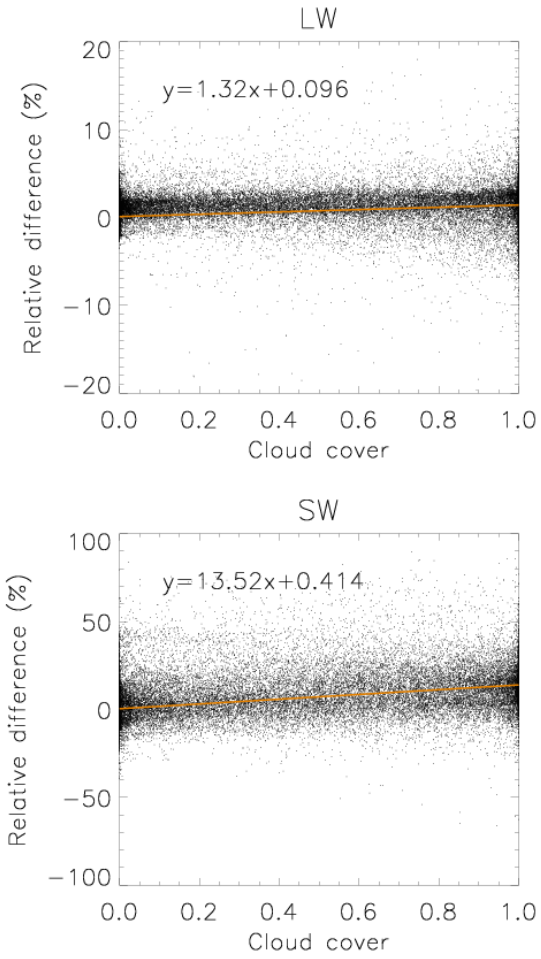

Fig. 14. Dependence of the CERES and SEVIRI relative difference on cloud cover.

AMTD
5, 4969–5008, 2012